# Velocity field and flow redistribution in a ballooned 7x7 fuel bundle measured by magnetic resonance velocimetry

Arthur Oliveira, Didier Stemmelen, Sebastien Leclerc, Tony Glantz, Alexandre Labergue, Georges Repetto, Michel Gradeck

# Velocity field and flow redistribution in a ballooned 7x7 fuel bundle measured by magnetic resonance velocimetry

A.V.S. Oliveira[a,b], D. Stemmelen[b], S. Leclerc[b], T. Glantz[a], A. Labergue[b], G. Repetto[a], M. Gradeck[b,*]

[a] *IRSN, PSN, B.P. 3, 13115 Saint Paul-Lez-Durance, France*
[b] *Université de Lorraine, CNRS, LEMTA, F-54000 Nancy, France*

**Abstract**

During a loss of coolant accident (LOCA), blocked sub-channels may appear due to the swelling of the fuel rods' cladding, which results in flow redistribution during the reflooding phase. For this reason, special attention has been paid to the effect of fuel rods ballooning on the thermal-hydraulics in LOCA conditions. Due to the practically impossible physical or optical access to blocked sub-channels, no experiment so far has performed precise three-component velocity field measurements in the presence of ballooned regions. In this study, we used magnetic resonance velocimetry (MRV) to obtain three-component velocity fields of water flow within two 7x7 fuel rods bundles built mainly in plastic, one regular and one containing sixteen ballooned fuel rods with 90% blockage ratio and 240 mm blockage length. We present herein results with 50 lpm water flow rate. With the regular bundle, the performance of spacer grids' mixing vanes to homogenize the flow was notable. With the ballooned bundle, we observed transverse velocities upstream of the ballooned zone that are as intense as the bulk mean velocity. Furthermore, there are substantial decreases in the axial velocity within blocked sub-channels up- and downstream of the ballooned zone, reaching near-zero and even negative values downstream, indicating flow recirculation. Although the flow is highly affected by the ballooned zone, the mixing spacer grid placed downstream remarkably homogenized the flow and effects of the flow redistribution disappeared. Finally, with the present ballooned bundle configuration, about 90% of the flow that should pass through blocked sub-channel deviates towards less resistant regions, which suggests a predominant geometric effect on the flow redistribution.

*Keywords:*
Magnetic resonance imaging, LOCA, Nuclear reactor, Clad ballooning, Thermal-hydraulics, Fluid dynamics

## 1. Introduction

During a hypothetical loss of coolant accident (LOCA) in a pressurized-water reactor (PWR), a subsequent evaporation and loss of water inventory may happen. The fuel rods' heat dissipation is enormously decreased and, by consequence, their claddings temperature increases, resulting in their ballooning or burst, as shown in Fig. 1 [1]. At this point, emergency core cooling systems (ECCS) inject water into the core to reflood the fuel assemblies and cool down the components. As the water level rises, steam and droplets are generated at the quenching front, providing a dispersed flow that plays a very important role to cool the regions that are not yet immersed into water. With that said and knowing that wall-to-steam convection is the predominant heat dissipation process in dispersed flow film

*Corresponding author
*Email address:* michel.gradeck@univ-lorraine.fr (M. Gradeck)

boiling [9, 10], the cooling in blocked sub-channels is highly degraded because of the preferential steam flow through intact or less blocked regions, which is known as flow redistribution or bypass effect [11].

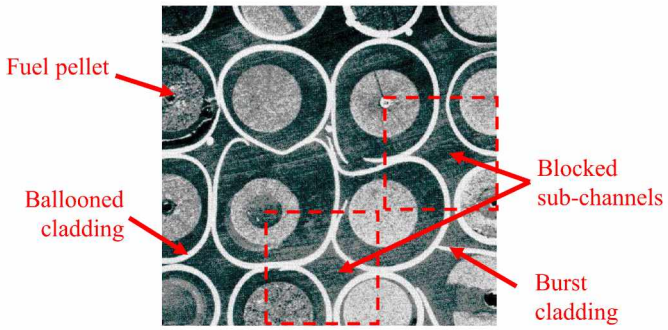


Figure 1: Fuel claddings and sub-channels after an in-pile LOCA experiment (adapted from [1]).

To guarantee nuclear safety, engineers must not only be capable of correctly estimating the flow dynamics and heat transfer in nuclear reactor's core thermal-hydraulics simulations but also understand the effects of components and geometrical irregularities. These tasks are truly difficult in LOCA conditions, where we have two-phase flow and a variety of heat and mass transfer phenomena [1]. Many studies have been carried out to improve the understanding of the nuclear reactor's core thermal-hydraulics in LOCA conditions, either with a regular fuel bundle [2, 3], with blockages due to clad ballooning [4, 5] and at sub-channel scale [6–8].

Grandjean mentions in his review of past experimental programs with ballooned fuel bundles that the blockage might be large and long enough that the fuel rod might no longer be coolable [12]. Moreover, those experiments showed that even the region downstream of the ballooned zone is affected by the flow redistribution because, depending on the blockage geometry and reflooding conditions, it is one of the hot-spots in the nuclear core. Hence, understanding how blocked sub-channels affect the steam flow is crucial to guarantee that all the fuel assemblies are cooled during a LOCA and, for this reason, this is still a topic that deserves attention and further investigation [13]. With that perspective, the French Institut de Radioprotection et de Sûreté Nucléaire (IRSN) launched the project PERFROI to better understand the thermal-mechanics and the thermal-hydraulics phenomena during a LOCA. With the main experiment in the thermal-hydraulics axis, which is named COAL [1], it is expected to obtain measurements during reflooding experiments in a partially ballooned 49-element bundle with electrically-heated fuel rods [14]. In fact, IRSN's code named DRACCAR [15, 16] was used to perform pre-simulations of the COAL experiments without validated models of flow redistribution [17, 18]. Hence, the results of this experimental work will be used to develop and validate such a model.

Measuring the flow dynamics in a fuel bundle is a challenge, especially with ballooned claddings that make access to blocked sub-channels virtually impossible. The use of physical sensors like Pitot tubes or hot wires disturbs the flow, while the use of optical techniques like PIV is not always feasible, although remarkable advances have been obtained using refractive index matching materials [19]. Thus, magnetic resonance velocimetry (MRV) becomes an excellent option to characterize the fluid dynamics in ballooned bundles because optical accesses or intrusive instruments and tracers are absolutely unnecessary. Furthermore, we can measure the three velocity components

[1] COAL: **CO**olability of a fuel **A**ssembly during **L**OCA

without moving the test section neither the equipment, which is convenient to have consistent velocity acquisitions at a given position. MRV is nearly the same method as the classic magnetic resonance imaging (MRI) largely used by the medical community, but with additional gradient pulses for the velocity encoding. Although this velocity measurement technique is already known for more than 30 years [20], its use in engineering has been more intensive in the last fifteen years as MRI scanners have become more accessible [21]. In nuclear engineering research, Piro et al used MRV to characterize the flow in a representative CANDU fuel bundle to validate numerical simulations [22]. They also affirmed the advantages of MRV for flow measurements in nuclear reactor geometries to evaluate fluid exchange between sub-channels and provide accurate measurements in constricted passages. Nevertheless, to the authors' knowledge, a detailed evaluation with MRV of the flow redistribution in the presence of blocked sub-channels has never been done before.

In this study, we used MRV to measure the velocity field of the water flow at several axial positions in two 7x7 bundles representative of a French PWR: one is regular and the other has sixteen ballooned rods. Both bundles were assembled using Inconel grids with the similar geometry and mixing structures as found in real PWR reactors. We analyzed the effect of mixing spacer grids on the flow characteristics, as well as the flow redistribution due to the presence of blocked sub-channels. Although we have performed experiments with four different flow rates, only velocity fields with the lowest flow rate (about 50 lpm) for each bundle are presented here. These experimental data are useful for the validation of simulation tools dedicated to nuclear safety analysis, such as DRACCAR.

## 2. MASCARA: experimental apparatus and procedure

### *2.1. Hydraulic circuit*

Figure 2 presents the experimental apparatus named MASCARA[2] built specifically for this experiment, consisting in a regular monophasic hydraulic circuit with approximately 80 liters of water. Safety solutions like electrovalves and by-passes are not presented in the figure to avoid clutter. We used an eccentric screw pump and a damper to ensure that we would have stable fluid flow within the test section throughout the MRV imaging period. An electromagnetic flowmeter with a 50 mm passage diameter measures the volumetric flow rate of water, which is important to validate the MRV measurements as we explain later. Moreover, we installed pressure transducers in the line to obtain the system pressure and the pressure drop on the circuit, which served mainly for monitoring and safety purposes.

In this study, we analyzed two different test sections, one named G0 representing an intact regular bundle, and the other with a ballooned region named G90%-240mm. Both are 7x7 bundles having forty-six tubes with 9.5 mm diameter to represent intact fuel rods and three tubes with a larger diameter (12.45 mm) to represent guide tubes. This assembly is very similar to the one designed for COAL experiments, except for the size of the housing (89 mm in this experiment, 94.1 mm in COAL). The cross-section of the regular zone is shown in Fig. 3 in the left, which corresponds to the cross-section all along the regular bundle. This cross-section also represents the rods in the ballooned bundle where they are all undamaged. However, in the ballooned zone (Fig. 4), sixteen rods have a shape as shown in Fig. 3 in the right to represent a blockage ratio of 90%. The blockage ratio $\tau_b$ is a common parameter

[2]MASCARA: **M**RI of **A**ssembly **S**ub-**C**hannels for the **A**nalysis of **R**eactor **A**ccidents

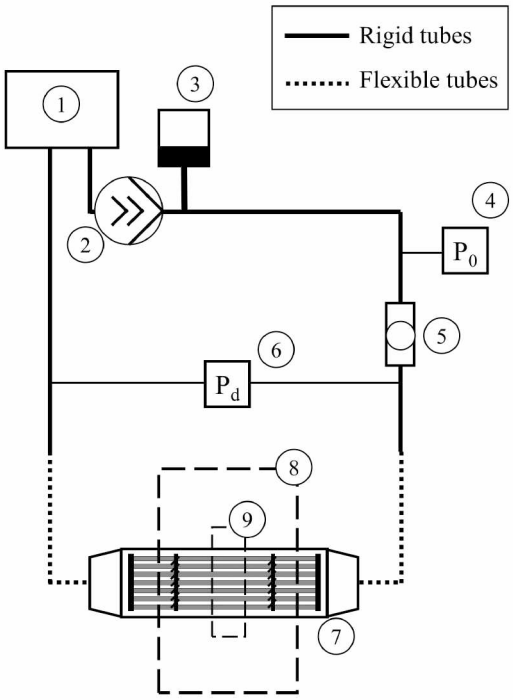


Figure 2: Hydraulic circuit of MASCARA: 1) water tank, 2) eccentric screw pump, 3) damper, 4) absolute pressure transducer, 5) electromagnetic flowmeter, 6) differential pressure transducer, 7) test section, 8) MRI scanner, 9) radiofrequency (RF) coil.

used in LOCA studies that indicates the decrease in the fluid passage cross-sectional area of a blocked sub-channel $S_b$ compared to an intact sub-channel $S_0$ (also shown in Fig. 3). This is mathematically defined as:

$$\tau_b = 1 - \frac{S_b}{S_0} \tag{1}$$

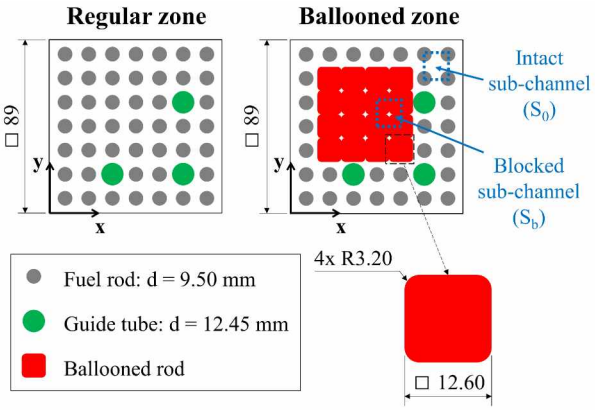


Figure 3: Cross-section illustration of each test section and their main dimensions.

Meanwhile, Fig. 4 presents the position of each grid used in the experiment along the z-direction, as well as the position and length of the ballooned zone in the ballooned bundle. At the two extremities, we find end-grids without mixing vanes, while the two in the middle are spacer grids with mixing vanes. Although the distances between the first two and the last two grids are slightly different between the bundles, the distance between the two mixing spacer

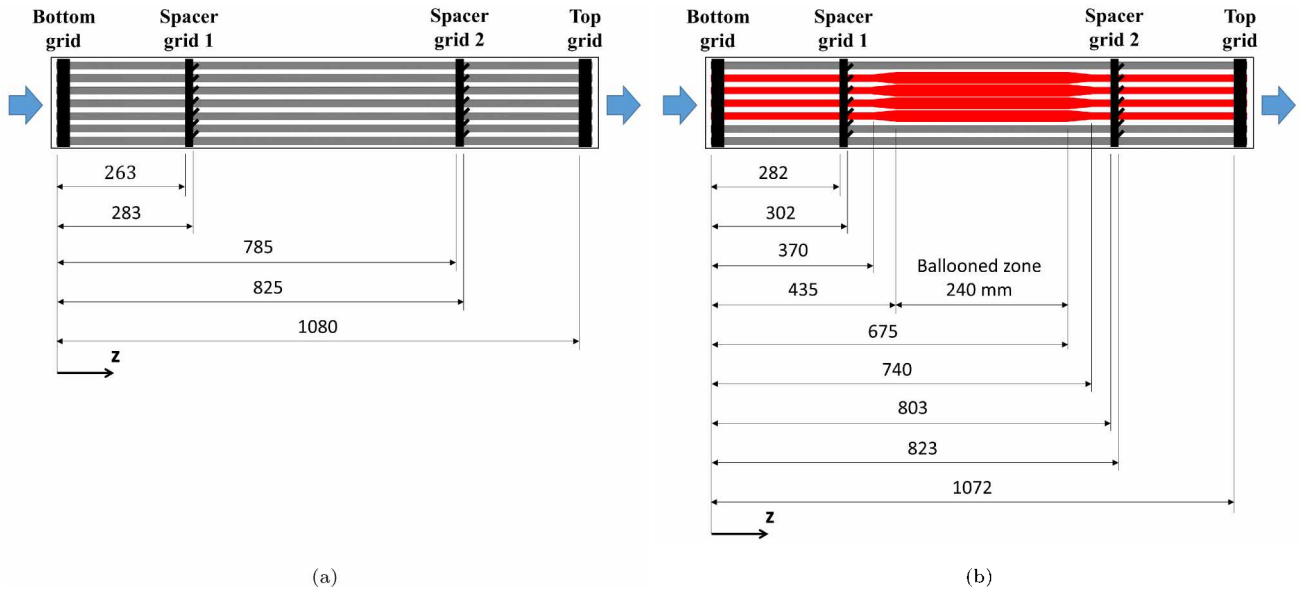


Figure 4: Side-view illustration of each test section and their main dimensions: (a) regular bundle (G0); (b) ballooned bundle (G90%-240).

grids in the middle, from rear face to rear face, is about 522 mm for both, which is the same distance found in a typical French PWR. To know the correct axial position during MRV measurements, capillary tubes were attached to the outer surface of the test section at specific and precise positions. Once the test section was placed inside the MRI scanner, these capillary tubes were found in preliminary signal intensity images before each MRV experiment using a spin-echo pulse sequence [23], which is the classic method used in medical imaging. Hence, their positions served as references to determine precisely the location of each selected slice for the velocity measurement.

It is important to comment on the transition from the regular to the ballooned zone found in the ballooned bundle, which is presented in Fig. 5. This smooth transition occurs in two parts. The first one is 35 mm long where the fuel rods cross-section increases, keeping the circular shape and without touching other rods. Consequently, fluid can flow from one sub-channel to another in this part. The second one is 30 mm long and starts at the point where the fuel rods touch each other and their cross-section deform progressively until reaching the shape shown in Fig. 3. This means that the flow passage cross-sectional area of blocked sub-channels decreases and fluid flow from one sub-channel to another is no longer possible. The transition zone finishes once the rods are fully deformed so, at this point, the ballooned zone begins. Downstream of the balloon there is another transition zone that is a mirror of the transition found upstream.

The materials used to build the test section are mainly plastic because no ferromagnetic material is allowed near or inside the MRI scanner. Hence, the intact fuel rods were made of polycarbonate tubes and the housing of acrylic slabs that were cut and glued together. Two aluminum parts were machined and mounted to the extremities of the housing so we could attach it to flexible tubes using quick-connectors. Because of its complex geometry, the ballooned zone was constructed by 3D-printing (FDM - fused-deposition modeling) using ABS as the base polymer. The four spacer grids are exactly the same that will be used in COAL experiments and they are made of Inconel, which is not a ferromagnetic material but still disturbs the magnetic fields, impeding us to perform MRV measurements closer than 4 cm to them.

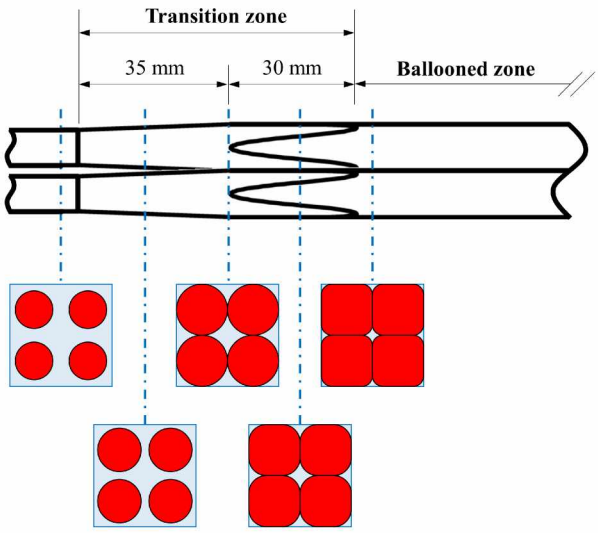


Figure 5: Transition from regular to ballooned zone.

We remind that, during a LOCA, the flow actually occurs with steam, not water. However, using steam in MRV experiments is not practical because the signal intensity is very low due to the low density of the vapor phase. Therefore, we performed the experiments with water, which provides much higher signals during an MRV, but conserving the same Reynolds number found with steam during a LOCA (between 1,000 and 10,000). Although we have tested several flow rates, the qualitative results for all the cases were very similar. For this reason, only the velocity fields with the lowest flow rate (about 50 lpm) are presented herein, which corresponds to a Reynolds number of 1936, therefore in the laminar regime.

### *2.2. MRV sequence and parameters*

We carried out MRI experiments using a Bruker Biospec Avance 24/40 mini-imager. This spectrometer is equipped with a 20 cm gradient coil delivering a 200 mT/m field gradient and a 16 cm Rapid Biomedical quadrature volume resonator. We used a classical gradient echo pulse sequence with additional bipolar gradient pulses in order to encode velocity (Fig. 6) [24] using the parameters presented in Table 1. In this experiment, the phase of a given voxel $\varphi$ is proportional to the velocity:

$$\varphi = \gamma \delta \Delta g V \tag{2}$$

with $\gamma$ being the gyromagnetic ratio of the nucleus, $\delta$ the gradient pulse duration, $\Delta$ the time interval between the centers of the two bipolar pulses, $g$ the gradient intensity, and $V$ the velocity. As a lot of factors can affect $\varphi$, like the fluid temperature or fields non-homogeneity, we usually acquire two consecutive images with two different gradient intensities (say $g_2$ and $g_1$) to take the phase difference between these two images. Consequently, we obtain a phase shift image $(\varphi_2 - \varphi_1)$ free of unwanted parametric effects and we can calculate the fluid velocity at a given location with the following expression

$$V = \frac{\varphi_2 - \varphi_1}{\gamma \delta \Delta (g_2 - g_1)} \tag{3}$$

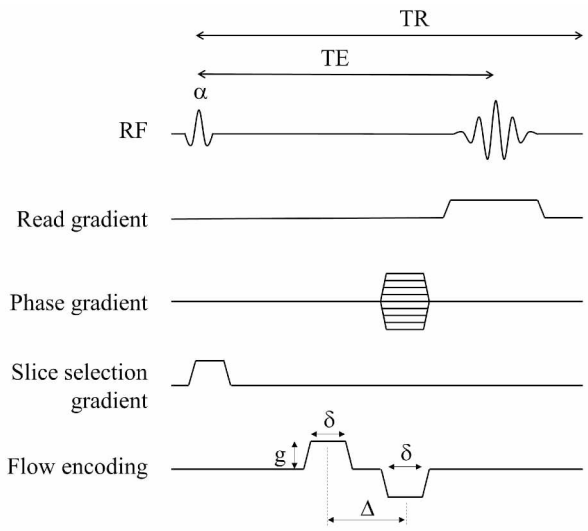


Figure 6: MRV sequence based on the gradient echo method with flow encoding gradients (RF: radiofrequency).

Table 1: Values of MRV parameters used in this study

| **PARAMETER** | **VALUE** |
|---|---|
| Flip angle ($\alpha$) | 30° |
| Number of accumulated images | 5 – 20 |
| Field-of-view | 120 mm |
| Matrix resolution | 256 x 256 pixels |
| Pixel resolution | 0.469 x 0.469 $mm^2$ |
| Repetition time (TR) | 15.0 ms |
| Echo time (TE) | 7.0 ms |

For convenience, $g_1$ is equal to zero. In its turn, the gradient intensity $g_2$ must be chosen carefully in order to ensure the phase shift is comprised between $-\pi$ and $+\pi$ to avoid phase aliasing. This is done by adjusting the velocity encoding parameter usually referred to as $VENC$, which is the maximum measurable velocity without having phase aliasing:

$$VENC = \frac{\pi}{\gamma \delta \Delta g_2} \tag{4}$$

In other words, the fluid velocity $V$ is equal to $VENC$ when $\varphi_2 - \varphi_1 = \pi$ and $V = -VENC$ when $\varphi_2 - \varphi_1 = -\pi$. As longitudinal and transverse velocities have different magnitudes in this study, the $VENC$ must be specifically chosen for the measurement of each velocity component. To avoid aliased velocity measurements, we used a VENC about 20% higher than the maximum velocity measured in the whole experiment.

*2.3. Image processing*

In this study, we had to use masking on the velocity field images for two main reasons: better visualization and proper data processing to correctly estimate the flow mean velocity. We can not simply calculate the mean value from the whole image because there are regions with water, where we are interested in, and others with solids, like the tubes and the housing. In a velocity field image, the location of solid-liquid interfaces is not evident without masking due to the flow no-slip condition on the walls, so we must find another way to differentiate the pixels that are located in water from those that are not.

One efficient method to create a mask is using a signal intensity field image at the same slice where MRV was performed because the signal intensity is proportional to water density. Actually, the same acquisition used for the MRV, which is based on the imaginary part of the signal, is re-processed to obtain a signal intensity field, this one based on the real part. Hence, we can define precisely where water is present, as well as the solid-liquid interface. Fig. 7 presents the image processing steps for better visualization of the masking methodology, using as example one result from a preliminary experiment. If masking were not used, we would have a noised image that would be difficult to analyze as shown in Fig. 7a. Then, this image is re-processed to obtain the signal intensity field image (Fig. 7b) that generates a binary image (Fig. 7c), which is the mask used in the original noised velocity field. The result is a cleaner velocity field image (Fig. 7c) presenting only the liquid phase that is appropriate for the flow analysis.

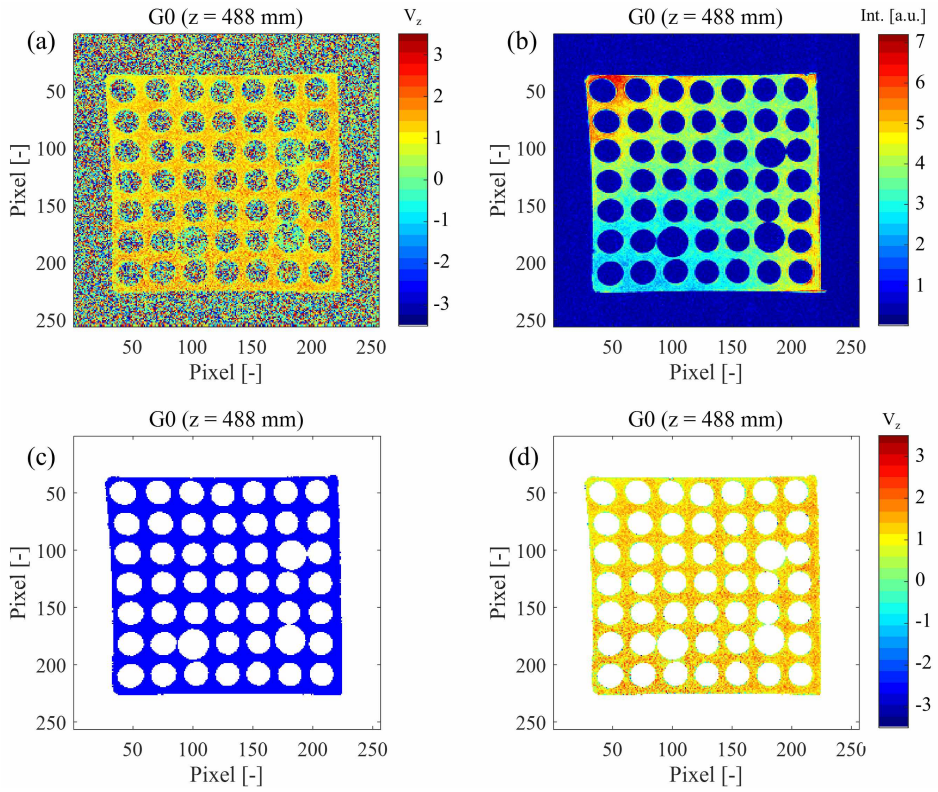


Figure 7: Example of the masking process with the regular bundle at z = 488 mm: (a) axial velocity field without masking; (b) signal intensity field image; (c) mask binary image; and (d) axial velocity field with masking.

Finally, transverse velocity fields (x and y-directions) are herein presented as vector plots to allow the simultaneous visualization of all the three velocity components in a single image. To transform an image in a vector plot, we divided

each sub-channel into several parts, as shown in Fig. 8. Those in the interior, like sub-channel A in the figure, were divided into four regions, while sub-channels near one wall (sub-channel B) or in the corners (sub-channel C) were divided into three and two parts, respectively. Then, we take the mean values of each transverse velocity for each part to create the velocity vector, whose origin is placed at the part's geometrical center. Eventually, we can combine the three velocity components in a single image as the example given in Figure 9, where the color bar refers to the magnitude of the axial velocity while arrows represent the direction and magnitude of the transverse velocity. All the three velocity components were normalized by the bulk mean axial velocity to better compare their intensities in the image.

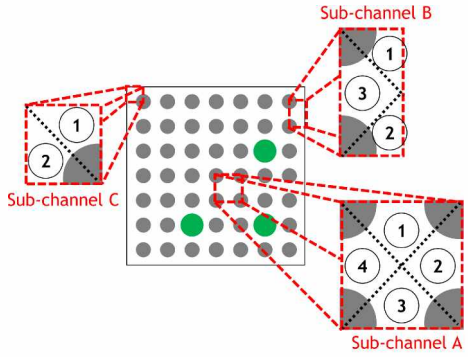


Figure 8: Sub-channel division to obtain the magnitude of transverse velocity vectors.

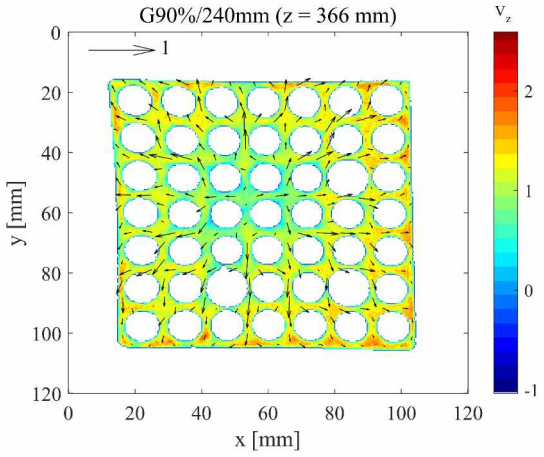


Figure 9: Example of a normalized three-component velocity field with the ballooned bundle at z = 366 mm.

### *2.4. Test procedure*

Having presented the experimental apparatus, the measurements techniques and the image processing, we introduce below the experimental procedure adopted in this study:

1. First, the test section was inserted into the MRI scanner. Then, after filling the hydraulic circuit with water, we started the pump and set its rotation velocity to supply approximately 250 lpm water flow rate for at least two minutes. Thus, bubbles attached to the test section walls were dragged and removed from the bundle. We also purged the air trapped at the highest points of the hydraulic circuit.

2. Then, we stopped the water flow by stopping the pump, so we could place the test section at the desired position and acquire signal intensity images to find a capillary tube, which was used as a reference for the MRV slice position.
3. At this point, we set the pump rotation frequency to provide the highest desired mass flow rate (about 240 lpm) and we started the data acquisition system to acquire data from the flowmeter. Then, we measured the three velocity components by MRV for all the slices using the method described in section 2.2. After, we reduced the pump velocity to the next desired flow rate and, again, MRV measurements were performed for the same slices. We repeated this step until covering all the desired flow rates.
4. Afterwards, the test section was re-positioned inside the MRI scanner for measurements in another axial location and steps 2 and 3 were repeated until covering all the desired locations along the test section.
5. Finally, all the images were collected and built as explained in sections 2.3 and data was processed as explained below in section 2.5.

### *2.5. Data processing, data reduction and uncertainties*

As mentioned, a flowmeter was used in the hydraulic circuit to validate the MRV results and its accuracy is 0.25% of the measurement. The volumetric flow rate $Q$ measured by this instrument allows calculating the bulk mean axial velocity $\widetilde{V}_{z,ref}$ with the following expression:

$$\widetilde{V}_{z,ref} = \frac{Q}{S_s(z)} \tag{5}$$

where $S_s$ is the total flow passage area in the test section at a given axial position $z$, which might be constant along the test section (in the case of the regular bundle) or not (for the ballooned bundle). This mean velocity is the value used in the image normalization mentioned in section 2.3 and is compared to another mean axial velocity $\widetilde{V}_{z,exp}$ that is calculated using MRV results by:

$$\widetilde{V}_{z,exp} = \frac{1}{N_{mask}} \sum_{i=1}^{N_{mask}} V_{z,exp,i}(x,y) \tag{6}$$

$N_{mask}$ being the number of pixels contained in the mask for a given axial position, as shown in Fig. 7c, and $V_{z,exp,i}$ the measured axial velocity for each pixel $i$. In perfect experimental and measurement conditions, those two mean velocities should match. Nevertheless, although using the MRV sequence shown in Fig. 6 should have suppressed undesired effects, several parameters still affect the fluid velocity measurements and a deterministic error might still be present. Figure 10 presents, for the regular bundle, the ratio of the mean velocities obtained by MRV and the flowmeter for each axial position of the test section and for all the tested flow rates. We find that most of the mean velocities obtained with MRV are within -10% and 20% deviation from the one obtained by the flowmeter.

Moreover, we observe a similar trend in the plot for all the flow rates and for each group of points collected for the same positioning of the test section inside the MRI scanner. This suggests the existence of a deterministic bias that can be corrected for the whole image. There are two possible sources for this bias: 1) the test section is relatively large with respect to the gradient coils size and, therefore, we can see effects of the gradients non-linearity defaults; and 2) the presence of large aluminum bodies in the extremities that also disturb the magnetic fields. Considering this bias uniform in the whole velocity field for a given acquisition, we used a correction factor on all the

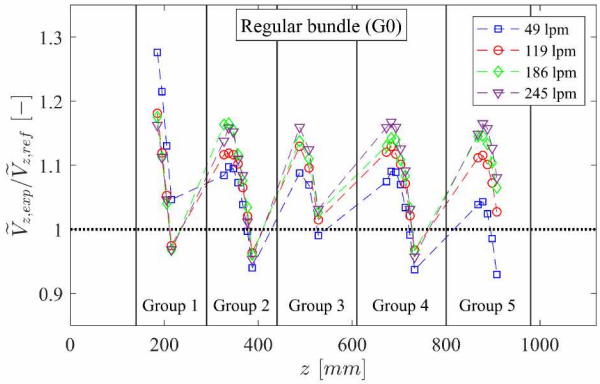


Figure 10: Comparison between the mean velocities obtained with MRV and the flowmeter.

pixels to ensure the mean fluid velocity calculated with Eq. 6 would match the one based on the flowmeter results (Eq. 5). Mathematically, this factor is the ratio of the mean axial velocities obtained with the flowmeter and the MRV measurements, hence:

$$V_{z,i}(x,y) = V_{z,exp,i}(x,y)\frac{\widetilde{V}_{z,ref}}{\widetilde{V}_{z,exp}} \qquad \forall\ i \tag{7}$$

and, with the results shown in Fig. 10, we find that the correction factor is within 0.83 and 1.15 for all the cases. For the transverse velocities, this normalization process is not possible because there is no referential measurement to correct its magnitude.

Estimating the velocity uncertainty at a specific pixel is not a simple and evident task [24], so one solution is using a statistical approach. As measurement errors in MRV appear due to random noises or in the magnitudes of magnetic fields and gradients or in electronic devices in the MRI scanner, we can consider this error $\varepsilon_V$ as addictive to the real velocity of the fluid $V_{real,i}$, resulting in our measurement $V_{exp,i}$ as given by the following expression:

$$V_{exp,i} = V_{real,i} + \varepsilon_V \tag{8}$$

hence, if we perform an MRV experiment in a stationary fluid ($V_{real} = 0$), we measure only the noise and we can evaluate the velocity uncertainty. Figure 11 presents the result of this experiment as a histogram of the measured axial velocity normalized by the used VENC (which was 50 cm/s in this example). We observe that the noise has a normal distribution with an average near zero, which means it is equally distributed, and a standard deviation of 4.4% of the VENC. Hence, we can affirm with 95% confidence that the measured velocity at each pixel lies within 9% of the used VENC [25]. Since we always set the VENC approximately 20% of the maximum velocity found in the measurement, as mentioned in section 2.2, the average velocity uncertainty for each pixel is approximately 20% of the mean bulk velocity. Although Fig. 11 presents one example for one VENC and for the axial velocity only, we found similar values for all VENC values and for all the three velocity components.

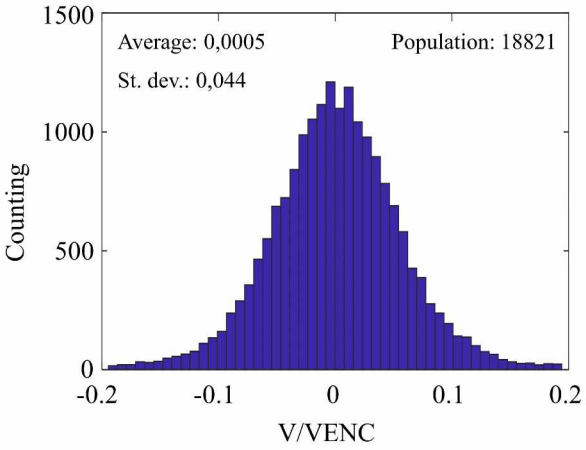


Figure 11: Histogram of the velocity measurement in a stationary fluid: example for the axial velocity with VENC = 50 cm/s.

## 3. Results and discussion

### *3.1. Regular bundle (G0)*

This section starts presenting in Fig. 12 velocity fields with the regular bundle at different axial positions, whose locations in the bundle are represented by letters in the schema over the images. As the fluid enters into the test section, the flow is not so homogeneous (Fig. 12a), which means that, as expected, the bottom spacer grid does not promote mixing of the fluid since it does not have mixing vanes. However, after passing through the first mixing spacer grid, the flow is homogenized by the mixing vanes, as we see in Fig. 12b with the appearance of transverse velocities. As the flow continues downstream of the first mixing spacer grid (Fig. 12c and d), these transverse velocities become negligible and also two regions with lower axial velocities appear near the housing upper and left walls. This might be explained by a slight decentralization of the bundle inside the housing so these regions have smaller flow passage areas than the sub-channels neighboring the opposite walls. Downstream of the second mixing spacer grid, the flow is once again homogenized (Fig. 12e).

### *3.2. Ballooned bundle (G90%-240mm)*

Velocity fields at different axial positions in the ballooned bundle are presented in Fig. 13. As well as done for the regular bundle, an illustration of the test section is given above the images to locate the position of each velocity field. The velocity field upstream of the first mixing spacer grid with the ballooned bundle is approximately the same of the observed with the regular bundle (Fig. 12a). Hence, this is not presented in Fig. 13 so we can concentrate the discussion on the flow redistribution due to the presence of ballooned fuel rods. Differently from the regular bundle, the flow behavior is particular for each location with this test section, so we should analyze the results by groups of images according to their axial position:

- *Downstream of the first mixing spacer grid and upstream of the ballooned zone (Fig. 13a-b)*: here we are at the transition zone, as shown in Fig. 5. Immediately after passing through the first mixing spacer grid, the flow should be homogeneous. However, the effect of the ballooned zone is already observed with the appearance of transverse velocities making the fluid deviate from blocked sub-channels (Fig. 13a). As the ballooned fuel

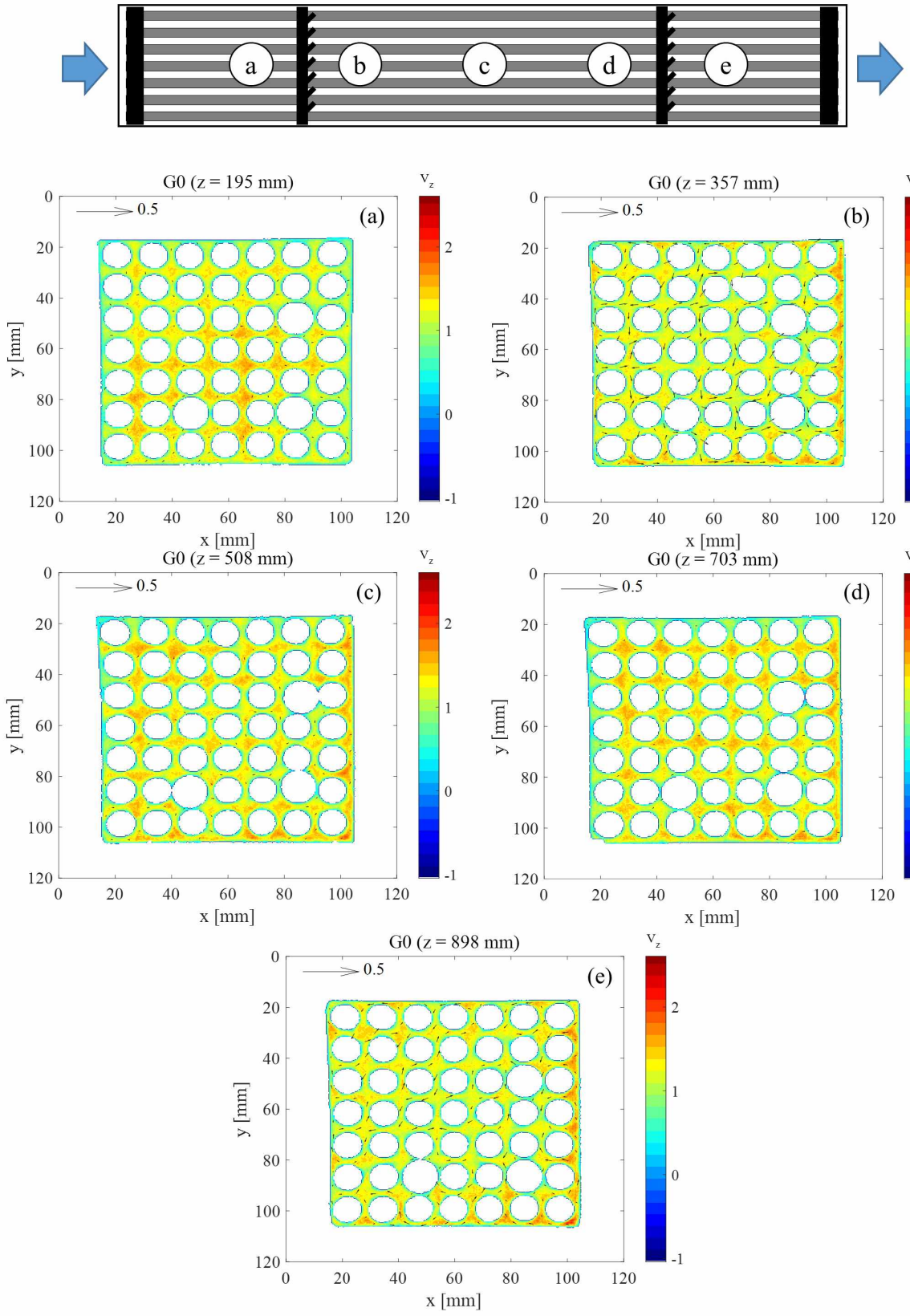


Figure 12: Velocity fields with the regular bundle.

rods enlarge, the transverse velocities are more intense, reaching nearly the same magnitude of the bulk mean velocity (Fig. 13b). The axial velocity decreases in blocked sub-channels while it increases in intact sub-channels, evidencing the flow redistribution due to the fuel rods ballooning.

- *In the ballooned zone (Fig. 13c)*: the axial velocity in blocked sub-channels is higher than the observed in the last image in the transition zone (Fig. 13b) due to the reduction in the flow passage area. Furthermore, the flow in blocked sub-channels is fully developed. Meanwhile, the fluid velocity in the other sub-channels are significantly higher than the bulk mean velocity due to the flow redistribution. Nevertheless, sub-channels neighboring the ballooned fuel rods, which are partially blocked because of the ballooning and the presence of guide tubes, have their axial velocity increased due to flow redistribution but not as much as in intact sub-channels. Transverse velocities are null in the blocked region and negligible between the other subchannels.

- *Downstream of the ballooned zone and upstream of the second mixing spacer grid (Fig. 13d-e)*: this is the second transition zone where the ballooned fuel rods' geometry recovers to the regular shape. As the flow passage area in blocked sub-channels re-increases, zero or even negative velocities appear near the walls, which indicates the presence of fluid recirculation. This particular result is discussed further. Consequently, the axial velocity in blocked sub-channels is substantially lower compared to the other sub-channels, which makes this region particularly critical during a LOCA as the fluid would hardly remove heat from the fuel rods due to its very low velocity. Furthermore, as soon as fluid exchanges between blocked sub-channels becomes possible and as their cross-sectional area enlarges, transverse velocities appear and increase in magnitude towards the center of the previously blocked sub-channels. Nevertheless, their magnitude is much lower than the observed upstream of the ballooned zone.

- *Downstream of the second mixing spacer grid (Fig. 13f)*: in spite of the large flow inhomogeneity caused by the ballooned zone as seen in Fig. 13e, the axial velocity field is remarkably homogenized by the second mixing spacer grid, suppressing any effect of the fluid deviation existent upstream. This is an important result showing that mixing spacer grids mitigate the ballooning effect on the flow and, therefore, play an important role to ensure nuclear safety in LOCA conditions.

As mentioned, we found near-zero and negative axial velocities downstream of the ballooned zone. Their presence is more evident when we look at Figure 14, which presents the velocity field at z = 740 mm in the ballooned bundle. The flow behavior is quite different for different flow rates at this position, so we present the velocity field in the two regimes: laminar (Re = 1936, which is the same for all the results presented before) and turbulent (Re = 7262). The bottom velocity fields are exactly the same presented in the top images, but the color bar comprises only negative values. In the laminar regime, the flow withing blocked sub-channels presents a maximum axial velocity at the center and very low velocities near the rods' walls, which is characteristic of a laminar flow. Nevertheless, we find substantial negative values around the four central ballooned fuel rods (up to 60% of the bulk mean velocity), which means there is intense flow recirculation at this location. On the other hand, we do not observe the peak velocity at center of blocked sub-channels in the turbulent regime, possibly because momentum diffusivity is much higher, as well as fluid mixing. Consequently, flow recirculation at this Reynolds number is less present and less intense, as presented in the bottom-right image in Fig. 14.

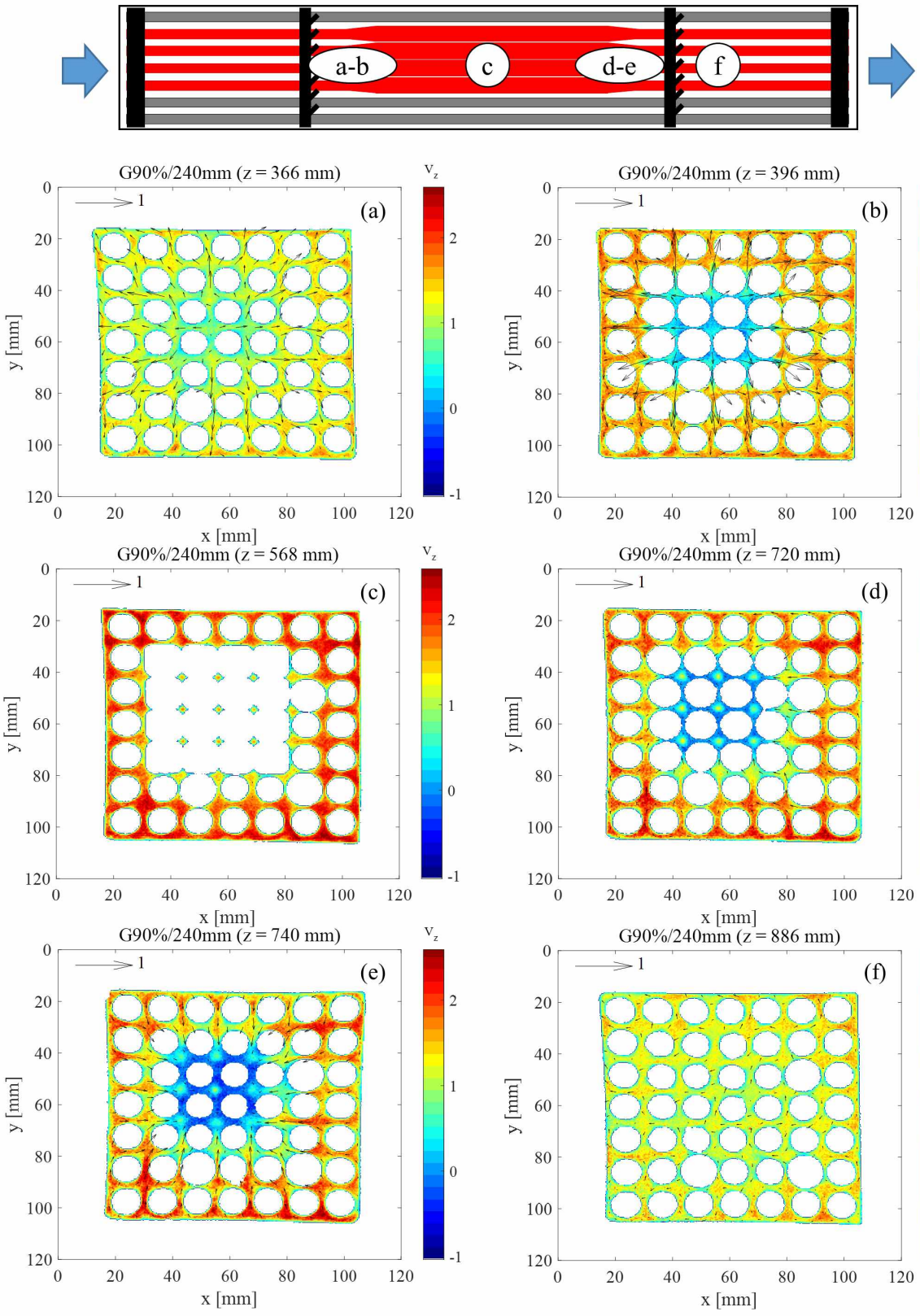


Figure 13: Velocity fields with the ballooned bundle.

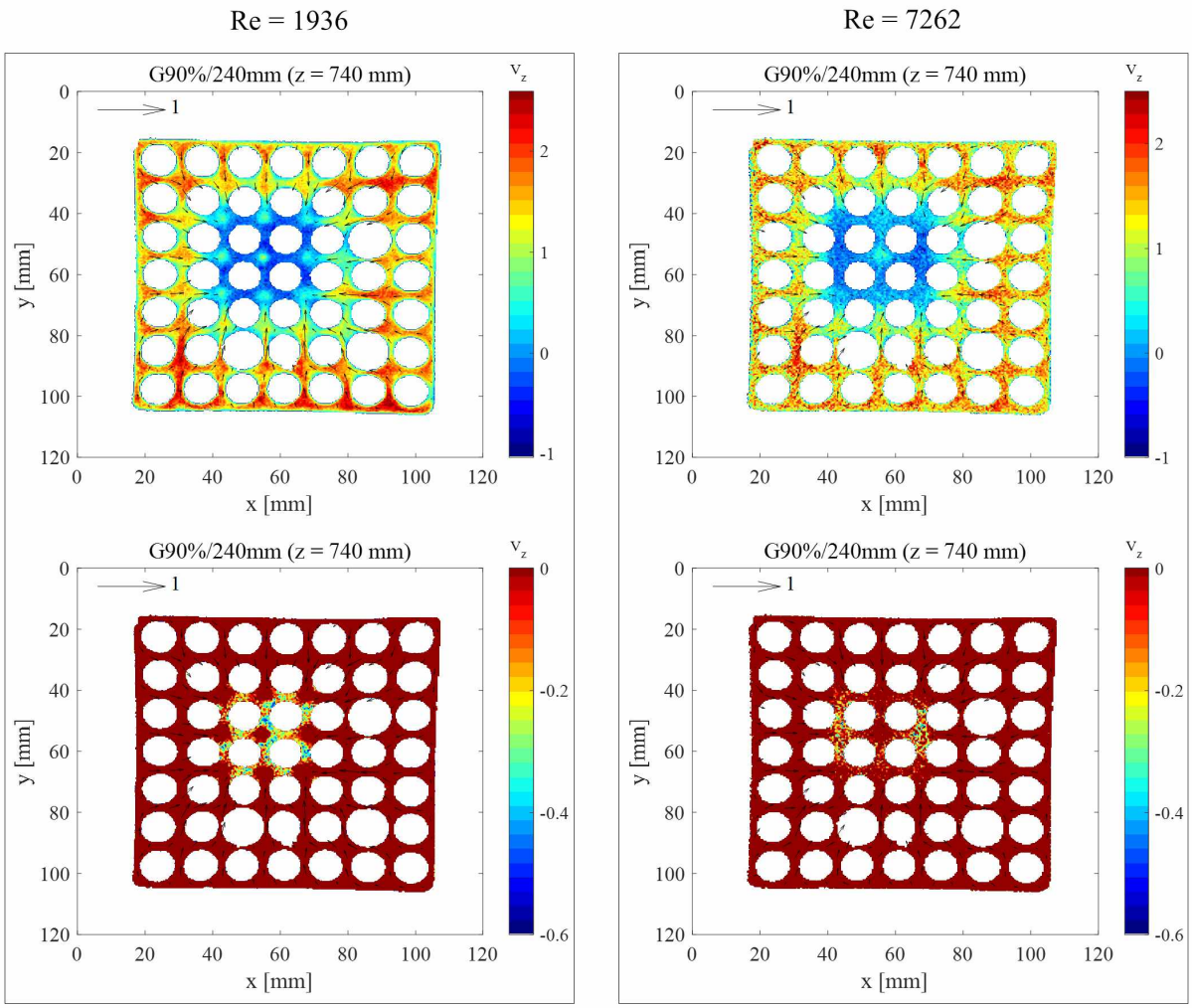


Figure 14: Velocity fields downstream of the ballooned zone with negative axial velocities in evidence.

With these results, we can estimate the amount of fluid that deviated from the blocked sub-channels. The ratio of deviated fluid $R_{dev}$ can be expressed by:

$$R_{dev} = 1 - \frac{\dot{m}_{sc,b}}{\dot{m}_{sc,r}} = 1 - \frac{\rho \widetilde{V}_{z,b} S_b}{\rho \widetilde{V}_{z,ref} S_0} \tag{9}$$

where $\dot{m}_{sc,b}$ and $\dot{m}_{sc,r}$ are the mass flow rates in a blocked sub-channel in ballooned and regular zones, respectively, $\rho$ is the water density (which is constant), and $\widetilde{V}_{z,b}$ the mean axial velocity in a blocked sub-channel. The fluid axial velocity in regular zones is considered the same as the mean bulk velocity entering the test section, i.e. $\widetilde{V}_{z,ref}$ at $z = 0$. Using Eq. 1 to have the blockage ratio $\tau_b$ in Eq. 9, we obtain:

$$R_{dev} = 1 - \frac{\widetilde{V}_{z,b}}{\widetilde{V}_{z,ref}} (1 - \tau_b) \tag{10}$$

As $\widetilde{V}_{z,b}$ is between 40% and 90% of $\widetilde{V}_{z,ref}$, the amount of deviated flow is slightly higher than 90%. Hence, the blockage ratio plays an important role on the flow redistribution with the present ballooned bundle configuration.

## 4. Conclusions

This study presented experimental results of water flow in two 1 m long 7x7 bundles, whose dimensions were based on a typical French pressurized-water reactor (PWR). While the first is a intact regular bundle, the second has a ballooned zone with 90% blockage ratio and 240 mm long between two mixing spacer grids. Magnetic resonance velocimetry (MRV) was used to measure the three velocity components of the fluid at several axial positions. Due to limitations regarding the measurement technique, the test section was entirely built in plastic and paramagnetic materials.

With the regular bundle, the role of mixing spacer grids to homogenize the fluid flow was evident. The mixing vanes produce transverse velocities that increase the fluid exchange between the sub-channels; however, the magnitude of these transverse velocities decreases along the flow direction, being negligible when reaching the second mixing spacer grid. Furthermore, the fluid axial velocity decreases in sub-channels neighboring the housing walls because of their smaller cross-sectional area.

With the ballooned bundle, the fluid deviation from blocked sub-channels is already visible at the beginning of the transition from the regular to the ballooned zones. Transverse velocities appear and their intensity increases while the ballooned fuel rods are not in contact, reaching magnitudes in the same order of the bulk mean velocity. The axial velocity in blocked sub-channels decreases and then increases in the transition before the ballooned zone. In the ballooned zone, the axial velocity was higher in intact sub-channels but not as much in those neighboring the balloon and containing guide tubes. Downstream of the balloon, recirculating zones appear around ballooned fuel rods and the mean axial velocity in blocked sub-channels decreases enormously due to the increase of the flow passage area, reaching near-zero values. This fluid recirculation is less intense in the turbulent regime. Also, still downstream of the ballooned zone, transverse velocities appear towards the blocked sub-channels as it was redistributing the deviated flow, but the magnitude of these velocities is much lower than the observed upstream of the balloon. Nevertheless, after passing through the second mixing spacer grid, the flow is remarkably homogenized by the mixing vanes and the effect of the ballooned zone is no longer existent. Finally, the amount of deviated flow from blocked sub-channels was estimated to be slightly higher than the blockage ratio, suggesting a predominant effect of the geometry on the flow redistribution.

## 5. Funding

This work is completed within the framework of RSNR Project PERFROI from a French State aid managed by the French National Research Agency under the program of Investments for the Future carrying the reference n° ANR-11-RSNR-0017.

## References

[1] G. Repetto, C. Dominguez, B. Durville, S. Carnemolla, D. Campello, C. Tardif, M. Gradeck, The R&D PERFROI project on thermal mechanical and thermal hydraulics behaviors of a fuel rod assembly during a loss of coolant accident, 16th International Topical Meeting on Nuclear Reactor Thermal Hydraulics (NURETH-16) 1 (2015) 1–14.

[2] Y. Jin, F.-B. Cheung, S. M. Bajorek, K. Tien, C. L. Hoxie, Investigation of the thermal-hydraulic non-equilibrium in a 7x7 rod bundle during reflood, International Journal of Heat and Mass Transfer 127 (2018) 266 – 279. doi:https://doi.org/10.1016/j.ijheatmasstransfer.2018.08.011.

[3] Y. Jin, F. R. Beck, B. R. Lowery, D. J. Miller, F. B. Cheung, S. M. Bajorek, K. Tien, C. L. Hoxie, Experimental study of droplet sizes across a spacer grid location under various reflood conditions, Experimental Thermal and Fluid Science 94 (February 2017) (2018) 246–257. doi:10.1016/j.expthermflusci.2018.02.017.

[4] J. Kim, S. Cho, J.-K. Park, Y.-J. Youn, S.-K. Moon, Experimental study to assess effects of ballooning and fuel relocation on the coolability of fuel rod bundle, Nuclear Engineering and Design 332 (2018) 1 – 10. doi:https://doi.org/10.1016/j.nucengdes.2018.03.013.

[5] Z. Hózer, I. Nagy, M. Kunstár, P. Szabó, N. Vér, R. Farkas, I. Trosztel, A. Vimi, Experimental investigation of the coolability of blocked hexagonal bundles, Nuclear Engineering and Design 317 (2017) 51 – 58. doi:https://doi.org/10.1016/j.nucengdes.2017.03.030.

[6] A. V. S. Oliveira, J. D. Peña Carrillo, A. Labergue, T. Glantz, M. Gradeck, Experimental study of dispersed flow film boiling at sub-channel scale in loca conditions: Influence of the steam flow rate and residual power, Applied Thermal Engineering 172 (2020) 115143. doi:https://doi.org/10.1016/j.applthermaleng.2020.115143.

[7] J. D. Peña Carrillo, A. V. S. Oliveira, A. Labergue, T. Glantz, M. Gradeck, Experimental thermal hydraulics study of the blockage ratio effect during the cooling of a vertical tube with an internal steam-droplets flow, International Journal of Heat and Mass Transfer 140 (2019) 648 – 659. doi:https://doi.org/10.1016/j.ijheatmasstransfer.2019.06.012.

[8] K. Kim, B. J. Kim, H. S. Choi, S. K. Moon, C. H. Song, Effect of a blockage length on the coolability during reflood in a 2 x 2 rod bundle with a 90% partially blocked region, Nuclear Engineering and Design 312 (2017) 248–255. doi:10.1016/j.nucengdes.2016.08.031.

[9] A. V. S. Oliveira, J. D. Peña Carrillo, A. Labergue, T. Glantz, M. Gradeck, Mechanistic modeling of the thermal-hydraulics in polydispersed flow film boiling in loca conditions, Nuclear Engineering and Design 357 (2020) 110388. doi:https://doi.org/10.1016/j.nucengdes.2019.110388.

[10] Y. Guo, K. Mishima, A non-equilibrium mechanistic heat transfer model for post-dryout dispersed flow regime, Experimental Thermal and Fluid Science 26 (6-7) (2002) 861–869. doi:10.1016/S0894-1777(02)00195-4.

[11] P. Ruyer, N. Seiler, B. Biton, F. Lelong, F. Secondi, D. Baalbaki, M. Gradeck, Two-phase flow across a partially damaged core during the reflood phase of a loca, Nuclear Engineering and Design 264 (2013) 187 – 194, sI:NURETH-14. doi:https://doi.org/10.1016/j.nucengdes.2013.02.026.

[12] C. Grandjean, Coolability of blocked regions in a rod bundle after ballooning under loca conditions: Main findings from a review of past experimental programmes, Nuclear Engineering and Design 237 (15) (2007) 1872 – 1886, NURETH-11. doi:https://doi.org/10.1016/j.nucengdes.2007.02.022.

[13] C.-H. Song, Some issues and challenges in advanced thermal-hydraulic safety research, Nuclear Technology 196 (3) (2016) 421–445. doi:https://doi.org/10.13182/NT16-91.

[14] G. Repetto, C. Marquié, B. Bruyère, T. Glantz, Core coolability in loss of coolant accident: the COAL experiments, 16th International Topical Meeting on Nuclear Reactor Thermal Hydraulics (NURETH-16) 1 (2015) 24–37.

[15] T. Glantz, T. Taurines, S. Belon, O. D. Luze, G. Guillard, F. Jacq, Draccar: A multi-physics code for computational analysis of multi-rod ballooning, coolability and fuel relocation during loca transients. part two: Overview of modeling capabilities for loca, Nuclear Engineering and Design 339 (2018) 202 – 214. doi:https://doi.org/10.1016/j.nucengdes.2018.08.031.

[16] T. Glantz, T. Taurines, O. D. Luze, S. Belon, G. Guillard, F. Jacq, Draccar: A multi-physics code for computational analysis of multi-rod ballooning, coolability and fuel relocation during loca transients. part one: General modeling description, Nuclear Engineering and Design 339 (2018) 269 – 285. doi:https://doi.org/10.1016/j.nucengdes.2018.06.022.

[17] G. Repetto, T. Glantz, G. Guillard, B. Bruyère, Q. Grando, Core coolability in loss of coolant accident: the COAL experiments investigating the thermal hydraulics of a rod bundle with blocked area during the reflooding, 17th International Topical Meeting on Nuclear Reactor Thermal Hydraulics (NURETH-17) 1 (2017) 359–372.

[18] G. Repetto, B. Bruyère, S. Eymery, T. Glantz, Thermal hydraulics behavior of a rod bundle with partially blocked area during the reflooding phase of the loss of cooling accident, 11th International Topical Meeting on Nuclear Reactor Thermal-Hydraulics, Operation and Safety (NUTHOS-11) 1 (2016) 1.

[19] A. A. Campagnole dos Santos, M. Childs, T. D. Nguyen, Y. Hassan, Convergence study and uncertainty quantification of average and statistical piv measurements in a matched refractive index 5x5 rod bundle with mixing vane spacer grid, Experimental Thermal and Fluid Science 102 (2019) 215 – 231. doi:https://doi.org/10.1016/j.expthermflusci.2018.11.009.

[20] E. Fukushima, Nuclear magnetic resonance as a tool to study flow, Annual Review of Fluid Mechanics 31 (1) (1999) 95–123. arXiv:https://doi.org/10.1146/annurev.fluid.31.1.95, doi:10.1146/annurev.fluid.31.1.95.
URL https://doi.org/10.1146/annurev.fluid.31.1.95

[21] L. F. Gladden, A. J. Sederman, Magnetic resonance imaging and velocity mapping in chemical engineering applications, Annual Review of Chemical and Biomolecular Engineering 8 (1) (2017) 227–247. doi:10.1146/annurev-chembioeng-061114-123222.

[22] M. Piro, F. Wassermann, S. Grundmann, B. Tensuda, S. Kim, M. Christon, M. Berndt, M. Nishimura, C. Tropea, Fluid flow investigations within a 37 element CANDU fuel bundle supported by magnetic resonance velocimetry and computational fluid dynamics, International Journal of Heat and Fluid Flow 66 (2017) 27 – 42. doi:https://doi.org/10.1016/j.ijheatfluidflow.2017.04.010.

[23] M. Bernstein, K. King, X. Zhou, Handbook of MRI Pulse Sequences, Elsevier Science, 2004.

[24] C. Elkins, M. Markl, A. Iyengar, R. Wicker, J. Eaton, Full-field velocity and temperature measurements using magnetic resonance imaging in turbulent complex internal flows, International Journal of Heat and Fluid Flow 25 (5) (2004) 702 – 710, selected papers from the 4th International Symposium on Turbulence Heat and Mass Transfer. doi:https://doi.org/10.1016/j.ijheatfluidflow.2004.05.017.

[25] R. J. Moffat, Describing the uncertainties in experimental results, Experimental Thermal and Fluid Science 1 (1) (1988) 3 – 17. doi:http://dx.doi.org/10.1016/0894-1777(88)90043-X.